String phase driven reconfigurable magnonics in Santa Fe ice

Amrit Kumar Mondal [1,*] and Anjan Barman [1,2,†]

[1] *Technical Research Centre, S. N. Bose National Centre for Basic Sciences, Block JD, Sector III, Salt Lake, Kolkata 700106, India*

[2] *Department of Condensed Matter and Materials Physics, S. N. Bose National Centre for Basic Sciences, Block JD, Sector III, Salt Lake, Kolkata 700106, India*

(Received 5 February 2024; accepted 3 May 2024; published 17 May 2024)

The existence of one-dimensional strings of local excitations represents an intriguing aspect of the properties of strongly correlated topological quantum matter. Here, we study the impact of these one-dimensional string phases (1D SPs) on magnetization dynamics in Santa Fe ice lattice using micromagnetic simulations. The presence of 1D SPs results in the creation of parallel configurational anisotropic doublet or triplet pairs of spin wave (SW) modes, attributed to distinct stray field distributions. These modes induce the formation of an anticrossing gap in both reciprocal and nonreciprocal SW dispersion that can be experimentally measured.

DOI: 10.1103/PhysRevB.109.184433

I. INTRODUCTION

Strongly correlated many-body systems exhibit intriguing exotic phenomena [1], even with simple underlying interactions. Artificial spin ice (ASI) arrays [2–8], composed of coupled single-domain nanomagnets, exemplify this class of systems. Santa Fe ice (SFI) is one of the exotic designs within the ASI family [1,4,9,10] which has emerged as a promising avenue for investigating magnetic frustration and its unique properties. Here each vertex can represent a frustrated unit, as the arrangement of magnetic moments at these vertices naturally resists traditional ordering. The study of exotic magnetism via frustration and topology has led to valuable insights into the characterization of frustrated magnetic systems and offers a unique opportunity to explore the properties of emergent quasiparticles [1–4,9,10]. For the last few decades, the studies of this frustration in simple square and kagome ASI lattices have revealed their significant influences on both the equilibrium behavior and magnetization reversal dynamics [5,11,12]. The lowest-energy ground state in both square and kagome lattices are achievable, where all vertices are in their optimal local energy states [13–19]. However, in any SFI lattice, some of the vertices are always in a nonoptimal local energy state, despite being in the collective ground state. These nonoptimal vertices are commonly referred to as "unhappy" vertices [1,4,9,10]. This geometric constraint forces unhappy vertices to create one-dimensional (1D) string phases (SPs), which may terminate within inner plaquettes or create closed loops. Zhang *et al.* demonstrated that SP descriptions and related topological features are not exclusive to quantum models; they also offer a simplified description of complex classical systems with nontrivial frustration [9,10]. Recently, experimental efforts have shown the direct visualization of topologically constrained kinetics in an SFI array [9]. Recent numerical simulations further show the significance of vortex configurations, pinning, and flow patterns in a system with an SFI geometry [20]. An interesting question is whether the presence of such 1D SPs affects the reconfigurable spin wave (SW) dynamics of the spin-ice lattice. The creation of such a prototype holds significant potential for diverse applications, including the advancement of novel memory solutions, quantum computing, and neuromorphic computing systems [8,10,14,21,22].

In this work, we aim to isolate the role of 1D SP on magnetization dynamics in the SFI lattice made of $Ni_{80}Fe_{20}$ (permalloy, Py hereafter) elongated nanobars with rounded ends. Here, we design two distinct 1D SP model SFI lattices along with another reference state (RS) of SFI lattice with no SP, resulting in three distinct magnetic microstates. We observe a significant difference in uncompensated magnetic charges in their stray field distribution. As a result, rich SW spectra (frequencies: f) are observed in those systems and detailed SW dispersions with both bias field strength (H) and orientation (φ) have been studied. These three microstates provide rich magnonic spectra with precise control in SW frequency shift from symmetric to an asymmetric field (f vs H) dispersion, configurational anisotropic parallel mode creation, mode hybridization, and magnon-magnon coupling. These 1D strings of local excitations are an important characteristic in strongly correlated topological quantum matter, and our result demonstrates their reconfigurability in magnetization dynamics.

II. RESULTS AND DISCUSSION

We examined the magnetization dynamics in an SFI lattice, comprising 112 Py elements, each with dimensions of $340 \times 120 \times 20\ \text{nm}^3$, as shown in Fig. 1(a). To simulate this system, we employed the mumax3 simulator [23] and discretized the samples into cuboidal cells measuring $4 \times 4 \times 20\ \text{nm}^3$. The material parameters for Py were set as follows: $A = 13\ \text{pJ/m}$ (exchange constant), $M_s = 840\ \text{kA/m}$ (saturation magnetization), and $K = 0$ (magnetocrystalline anisotropy) [24,25]. Further, we employed periodic boundary conditions (PBCs) (2, 2, 0) in our simulations to eliminate

*amritphysics2017@gmail.com
†abarman@bose.res.in

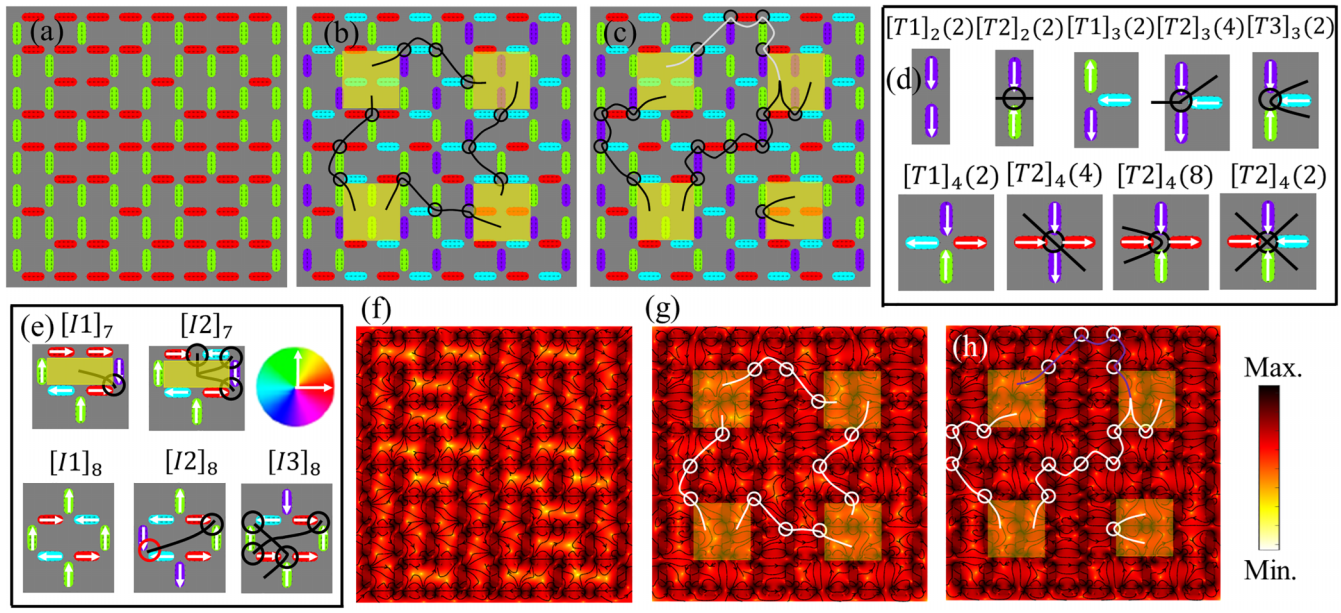

FIG. 1. A complete unit cell illustrating the ground states of the Santa Fe ice lattice. The schematic representation of the moment configurations and the string phases (SP) for the reference state (RS) (a), and two representative models of disordered string ground states, namely SP-I and SP-II (b),(c). (d) The vertex moment configurations are organized in ascending energy order. $[Tn]_m(p)$ denotes the "type-n" artificial spin ice (ASI) constructed by "m" nanobars with "p" degeneracy ($n = 1, 2, 3, 4$ and $m = 2, 3, 4$). The black lines represent string segments, "connecting" the plaquettes through the unhappy vertices (black circles). (e) Some examples of moments and string configurations for peripheral (unshaded) and interior (yellow-shaded) plaquettes. $[In]_m$ denotes the nth unit plaquette of SFI constructed by m nanobars ($n = 1, 2 \ldots$ and $m = 7, 8$). The arrows indicate the direction of moment. (f)–(h) The stray field distribution in RS, SP-I, and SP-II states.

edge effects. We prepared an RS of the lattice by saturating the array along the (100) direction for $\varphi = 0^\circ$ [$(\cos\varphi,\ \sin\varphi,\ 0)$ generalized direction for arbitrary φ] and adiabatically removing the external field. Subsequently, the system relaxes into a state where the magnetization aligns along the $+y$ direction for the vertical elements and along the $+x$ direction for the horizontal elements within the array [see Fig. 1(a)]. We further prepared two distinct models of SFI states (SP-I and SP-II) by tuning the unhappy vertices and subsequently relaxing the magnetization as represented in Figs. 1(b) and 1(c). Detailed discussions on the magnetic field histories for these three states can be found in Sec. A [Fig. S1(a)] of the Supplemental Material [26]. Here, the unhappy excited vertices are marked by black circles. Notably, they belong to different homotopy classes, as the interior plaquettes connected by strings are distinct. The simulated time-varying magnetization was run for 15 ns at 30-ps steps after applying a short perturbation of 0.2 mT for 20 ps. We also explored the individual grids, which were composed of two, three, or four moments [Fig. 1(d)], as well as a selection of model individual units formed by either seven or eight moments [Fig. 1(e)]. Here, $[Tn]_m(p)$ refers to the "type-n" ASI constructed by "m" nanobars with "p" degeneracy ($n = 1, 2, 3, 4$ and $m = 2, 3, 4$) and $[In]_m$ represents the nth unit plaquette of SFI constructed by "m" nanobars ($n = 1, 2 \ldots$ and $m = 7, 8$). The objective of this exploration was to gain a deeper understanding of how these elements contribute to the collective magnetization dynamics of SFI. To understand the stray field distribution of these three states [Figs. 1(f)–1(h)], we used our home-built MATLAB-based code DOTMAG [27].

Figures 2(a)–2(f) represent SW field dispersion for RS, SP-I, and SP-II states at $\varphi = 0^\circ$ and 45° over a range $+300\ \text{Oe} \geqslant H \geqslant -300\ \text{Oe}$ where these states remain intact. The complete SW field dispersion (+ saturation to − saturation) for all those states is shown in Fig. S2 of the Supplemental Material [26]. Here, we investigate various new SW modes by modifying these states. For RS, there are three dominating SW modes at $\varphi = 0^\circ$ [Fig. 2(a)] and four at $\varphi = 45^\circ$ [Fig. 2(d)]. The signature of magnon-magnon coupling in terms of anticrossing [25,28,29] is observed between $F1$ and $F3$ at $H = 30$ Oe for $\varphi = 0^\circ$ as well as between $F3$ and $F4$ at $H = -180$ Oe for $\varphi = 45^\circ$. We further observed mode softening [24,30] for the $F3$ mode at $H = 1000$ Oe at $\varphi = 0^\circ$ and $H = -97$ Oe at $\varphi = 45^\circ$. For SP-I, there are six dominating SW modes at $\varphi = 0^\circ$ [Fig. 2(b)] and four at $\varphi = 45^\circ$ [Fig. 2(e)], all of which show symmetry (reciprocal) with respect to $H = 0$ Oe. Specifically, $F2$ merges with $F1$, and $F3$ merges with $F4$ at $|H| \approx 32$ Oe when $\varphi = 0^\circ$. These doublet pairs, ($F1$, $F2$) and ($F3$, $F4$), exhibit strong repulsion at $H = 0$ Oe due to magnon-magnon coupling. Furthermore, an additional mode, $F2'$, emerges at $|H| = 185$ Oe. For $\varphi = 45^\circ$, $F2$ and $F3$ modes merge at $|H| = 100$ Oe, while the $F1$ and $F4$ modes exhibit an anticrossing behavior at $H = 0$ Oe. Notably, the slopes $(\partial f/\partial|H|)$ for the $F1$, $F2$, $F2'$, and $F5$ modes are positive, while the rest of the modes show negative slopes for SP-I. Furthermore, in the case of SP-II, we observe seven dominating SW modes at $\varphi = 0^\circ$ [Fig. 2(c)] and five at $\varphi = 45^\circ$ [Fig. 2(f)]. Among these modes, the slopes $(\partial f/\partial|H|)$ for $F1$, $F2$, $F3$, and $F7$ are positive, while the remainder exhibit negative slopes. At $\varphi = 0^\circ$, $F1$, $F2$,

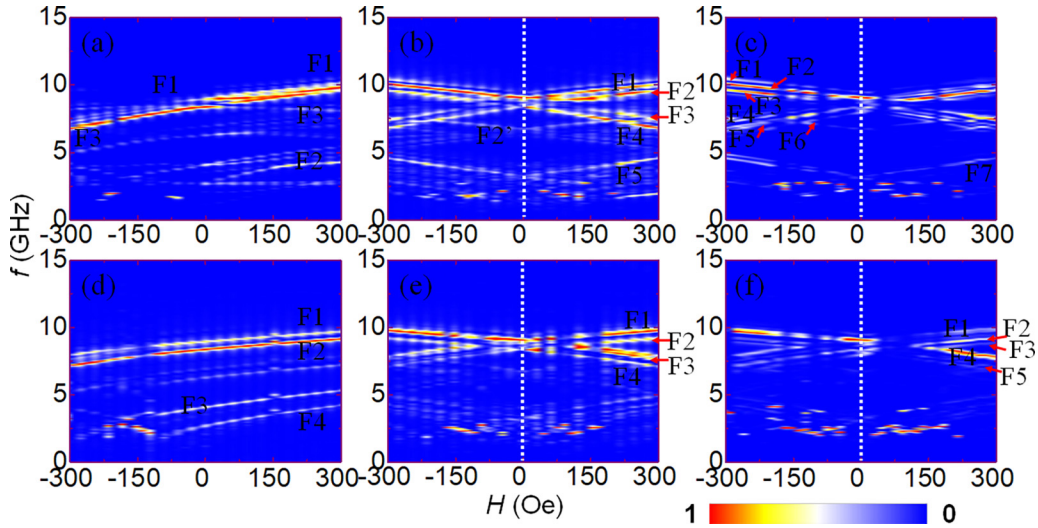

FIG. 2. (a)–(c) Surface plots of SW field dispersion for RS, SP-I, and SP-II states at $\varphi = 0°$. (d)–(f) Surface plots of SW field dispersion for RS, SP-I, and SP-II states at $\varphi = 45°$. The color map of the simulation result is shown at the bottom of the surface plots.

and $F3$ merge at $|H| \approx 55$ Oe, and similarly, $F4$, $F5$, and $F6$ merge at $|H| \approx 55$ Oe. Interestingly, these triplet pairs, ($F1$, $F2$, $F3$) and ($F4$, $F5$, $F6$), exhibit anticrossing at $H = 28$ Oe for $\varphi = 0°$. At $\varphi = 45°$, $F2$, $F3$, and F4 merge at $|H| \approx 105$ Oe, while the $F1$ and $F5$ exhibit an anticrossing behavior at $H \approx 50$ Oe. Additionally, between 35 and 120 Oe at $\varphi = 45°$, the intensity of edge modes within the range 1.8–2.2 GHz is significantly greater than that of other modes. That is why the SW mode between 7.5 and 9 GHz is not clearly visible in this range [Fig. 2(f)]. Importantly, all these modes in the SP-II state show antisymmetric (nonreciprocal) dispersion with respect to $H = 0$ Oe, primarily due to their 1D SP distribution. We also notice a significant presence of uncompensated magnetic charges in the RS [Fig. 1(f)]. However, as we move from SP-I to SP-II, there is a reduction in uncompensated magnetic charges [Figs. 1(g) and 1(h)], which results in an increased number of SW modes (Fig. 2). In the case of SP-I, the length of the 1D SP (equal to the number of unhappy vertices) remains the same for all four 1D SPs, allowing this state to achieve optimized uncompensated magnetic charges [Fig. 1(g)]. Consequently, all $F1$, $F2$, $F3$, and $F4$ modes in SP-I exhibit symmetric dispersion as shown in Figs. 2(b) and 2(e). Nevertheless, due to the nonuniform distribution of the number of unhappy vertices in the 1D SP in SP-II, we observe nonreciprocity in SW modes with respect to $H = 0$ Oe as shown in Figs. 2(c) and 2(f).

To gain a comprehensive insight into the configurational anisotropy of these three states, we conducted simulations of the angular dispersion (f vs φ) of SW at $H = 1200$ Oe (saturation) and $H = 300$ Oe (unsaturated region). At $H = 1200$ Oe, all states show identical angular dispersion [Fig. 3(a) and Figs. S1(b) and S1(c) of the Supplemental Material [26]] as they are in the same spin state. In this context, both the $F1$ and $F3$ display fourfold symmetry with opposite polarities. Figures 3(b)–3(d) show the angular dispersion of SWs for RS, SP-I, and SP-II states at $H = 300$ Oe. For RS, only $F1$ shows clear twofold angular dispersion, primarily attributed to its unique spin texture. In the case of SP-I, the doublet pairs ($F1$, $F2$) and ($F3$, $F4$) also display a twofold anisotropy with opposite polarity as shown in Fig. 3(c). Furthermore, for SP-II, the triplet pairs ($F1$, $F2$, $F3$) and ($F3$, $F4$, $F5$) similarly exhibit a twofold anisotropy with opposite polarity, as shown in Fig. 3(d). To explore the origin of the dominating doublet and triplet pairs, we have simulated the evolution of magnetization dynamics spectrum for $[Tn]_m(p)$ ($n = 1, 2, 3$ and $m = 2, 3$) and $[In]_m$ ($n = 1, 2, 3$ and $m = 7, 8$) at $H = 300$ Oe as represented in Figs. 4(a) and 4(b). For $[Tn]_m(p)$, three distinct positions (4.35, 6.5, and 8.15 GHz, highlighted by gray-shaded regions) in the magnetization spectrum are observed for the dominant three SW modes, with an exception for $[T1]_3(2)$, where primarily two low-frequency modes dominate around 2.5 and 3.2 GHz, as depicted in Fig. 4(a). Further, in case of $[In]_m$, we observed that all dominating modes are primarily located around two

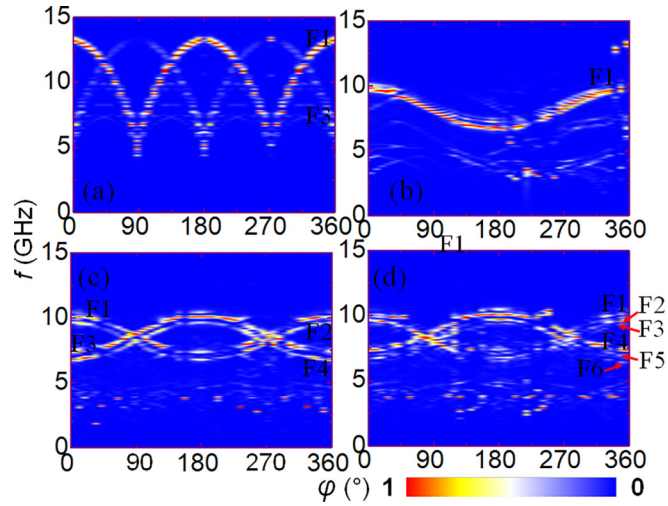

FIG. 3. (a) Surface plots of angular SW dispersion for RS at saturation ($H = 1200$ Oe). (b)–(d) Surface plots of angular SW dispersion for RS, SP-I, and SP-II states at unsaturated region ($H = 300$ Oe). The color map of the simulation result is shown at the bottom of the surface plots.

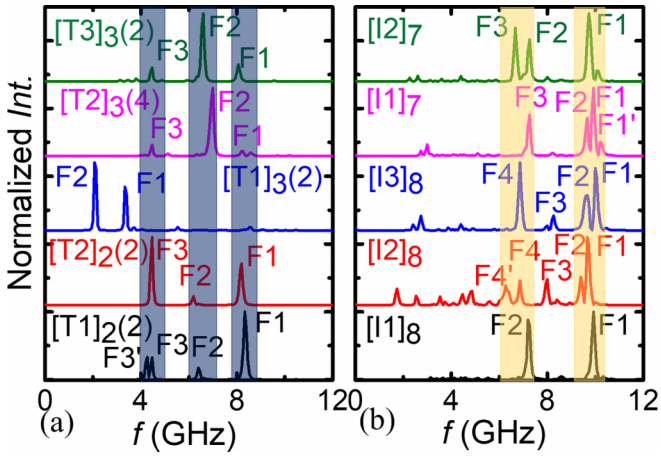

FIG. 4. (a)-(b) The evolution of SW spectrum for $[Tn]_m(p)$ ($n = 1, 2, 3$ and $m = 2, 3$) and $[In]_m$ ($n = 1, 2, 3$ and $m = 7, 8$) at $H = 300$ Oe. The shaded gray area indicates the potential dominant zone of SW modes for $[Tn]_m(p)$ ASI, while the shaded yellow region represents the likely dominant area of SW modes for various $[In]_m$ plaquettes within the SFI.

distinct positions (6.9 and 9.8 GHz, highlighted by yellow-shaded regions) in the SW spectrum [Fig. 4(b)]. Here, when the frequency gap between any two peaks, situated around 6.9 or 9.8 GHz ($f2$-$f1$), is less than spectral resolution, we notice a single resonant mode. However, when the spectral resolution is less than ($f2$-$f1$), we observe two prominent modes. Consequently, we can create doublet and triplet pairs in SW dispersion for SP-I and SP-II, resulting from the interaction of different SFI units. Additional interesting findings of doublet or triplet SW pairs located at 10 GHz within the SFI lattice are absent in $[Tn]_m(p)$, underlining the significance of the unit plaquette ($[In]_m$) in SW spectra of the SFI lattice. In this context, we note that the position of the SW spectra related to the string phase (∼7.8 and 10 GHz) differs from the SW spectra derived from ASI microstates (∼4.1, 6, and 8 GHz).

In summary, the existence and characteristics of the one-dimensional string phase (1D SP) in the Santa Fe ice (SFI) lattice significantly influence magnetization dynamics. These give rise to formation of the distinct configurational anisotropic parallel spin wave (SW) modes (doublet or triplet pairs), suggesting an experimental means to detect the 1D SP. Notably, the frequencies of these modes fall within the detectable range of experimental techniques like broadband ferromagnetic resonance (FMR) [18], and Brillouin light scattering (BLS) [31,32]. Starting from the RS state, we observe an anticrossing phenomenon arising from the interplay of distinct SW modes of single SFI units. Additionally, we explore an anticrossing gap caused by the interaction of different doublet or triplet SW pairs originating from distinct SFI units. Furthermore, we notice mode hybridization and the transition from symmetric to antisymmetric (reciprocal to nonreciprocal) behavior in SW field dispersion as the length of the SP varies. Here, we establish a correlation between the realization of complex string phases and the straightforward stray field distribution by providing direct visualization of 1D string phase-specific SW dynamics in SFI lattice. These findings open up exciting possibilities for influencing magnetization dynamics in such spin-ice lattices using factors like spin-polarized currents, spin textures, and nanobar dimensions, promising diverse applications in magnonics.

ACKNOWLEDGMENTS

A.B. gratefully acknowledges S. N. Bose National Centre for Basic Sciences, India, under Grant No. SNB/AB-RKM/21-22/280, and Nano Mission, Department of Science and Technology, Government of India, under Grant No. DST/NM/TUE/QM-3/2019-1C-SNB for funding. A.K.M. acknowledges the Technical Research Centre, S. N. Bose National Centre for Basic Sciences, India, for financial support.

[1] C. Nisoli, V. Kapaklis, and P. Schiffer, Deliberate exotic magnetism via frustration and topology, Nat. Phys. **13**, 200 (2017).
[2] S. Ladak, D. E. Read, G. K. Perkins, L. F. Cohen, and W. R. Branford, Direct observation of magnetic monopole defects in an artificial spin-ice system, Nat. Phys. **6**, 359 (2010).
[3] R. F. Wang, C. Nisoli, R. S. Freitas, J. Li, W. McConville, B. J. Cooley, M. S. Lund, N. Samarth, C. Leighton, V. H. Crespi and P. Schiffer, Artificial 'spin ice' in a geometrically frustrated lattice of nanoscale ferromagnetic islands, Nature (London) **439**, 303 (2006).
[4] M. J. Morrison, T. R. Nelson, and C. Nisoli, Unhappy vertices in artificial spin ice: New degeneracies from vertex frustration, New J. Phys. **15**, 045009 (2013).
[5] S. Gliga, E. Iacocca, and O. G. Heinonen, Dynamics of reconfigurable artificial spin ice: Toward magnonic functional materials, APL Mater. **8**, 040911 (2020).
[6] S. Sahoo, A. May, A. van Den Berg, A. K. Mondal, S. Ladak, and A. Barman, Observation of coherent spin waves in a three-dimensional artificial spin ice structure, Nano Lett. **21**, 4629 (2021).
[7] S. Gliga, A. Kákay, R. Hertel, and O. G. Heinonen, Spectral analysis of topological defects in an artificial spin-ice lattice, Phys. Rev. Lett. **110**, 117205 (2013).
[8] S. H. Skjærvø, C. H. Marrows, R. L. Stamps, and L. J. Heyderman, Advances in artificial spin ice, Nat. Rev. Phys. **2**, 13 (2020).
[9] X. Zhang, G. Fitez, S. Subzwari, N. S. Bingham, I.-A. Chioar, H. Saglam, J. Ramberger, C. Leighton, C. Nisoli, and P. Schiffer, Topological kinetic crossover in a nanomagnet array, Science **380**, 526 (2023).
[10] X. Zhang, A. Duzgun, Y. Lao, S. Subzwari, N. S. Bingham, J. Sklenar, H. Saglam, J. Ramberger, J. T. Batley, J. D. Watts, D. Bromley, R. V. Chopdekar, L. O'Brien, C. Leighton, C. Nisoli, and P. Schiffer, String phase in an artificial spin ice, Nat. Commun. **12**, 6514 (2021).
[11] M. T. Kaffash, S. Lendinez, and M. B. Jungfleisch, Nanomagnonics with artificial spin ice, Phys. Lett. A **402**, 127364 (2021).
[12] S. Lendinez and M. B. Jungfleisch, Magnetization dynamics in artificial spin ice, J. Phys.: Condens. Matter **32**, 013001 (2020).

[13] A. K. Chaurasiya, A. K. Mondal, J. C. Gartside, K. D. Stenning, A. Vanstone, S. Barman, W. R. Branford, and A. Barman, Comparison of spin-wave modes in connected and disconnected artificial spin ice nanostructures using brillouin light scattering spectroscopy, ACS Nano **15**, 11734 (2021).

[14] J. C. Gartside, K. D. Stenning, A. Vanstone, H. H. Holder, D. M. Arroo, T. Dion, F. Caravelli, H. Kurebayashi, and W. R. Branford, Reconfigurable training and reservoir computing in an artificial spin-vortex ice via spin-wave fingerprinting, Nat. Nanotechnol. **17**, 460 (2022).

[15] M. Taghipour Kaffash, W. Bang, S. Lendinez, A. Hoffmann, J. B. Ketterson, and M. B. Jungfleisch, Control of spin dynamics in artificial honeycomb spin-ice-based nanodisks, Phys. Rev. B **101**, 174424 (2020).

[16] V. S. Bhat, S. Watanabe, K. Baumgaertl, A. Kleibert, M. A. W. Schoen, C. A. F. Vaz, and D. Grundler, Magnon modes of microstates and microwave-induced avalanche in kagome artificial spin ice with topological defects, Phys. Rev. Lett. **125**, 117208 (2020).

[17] V. S. Bhat, F. Heimbach, I. Stasinopoulos, and D. Grundler, Magnetization dynamics of topological defects and the spin solid in a kagome artificial spin ice, Phys. Rev. B **93**, 140401(R) (2016).

[18] M. B. Jungfleisch, J. Sklenar, J. Ding, J. Park, J. E. Pearson, V. Novosad, P. Schiffer, and A. Hoffmann, High-frequency dynamics modulated by collective magnetization reversal in artificial spin ice, Phys. Rev. Appl. **8**, 064026 (2017).

[19] X. Zhou, G.-L. Chua, N. Singh, and A. O. Adeyeye, Large area artificial spin ice and anti-spin ice $Ni_{80}Fe_{20}$ structures: Static and dynamic behavior, Adv. Funct. Mater. **26**, 1437 (2016).

[20] W. Li, C. J. O. Reichhardt, B. Jankó, and C. Reichhardt, Vortex ordering and dynamics on Santa Fe artificial ice pinning arrays, Appl. Phys. Lett. **118**, 162601 (2021).

[21] J. Grollier, D. Querlioz, K. Y. Camsari, K. Everschor-Sitte, S. Fukami, and M. D. Stiles, Neuromorphic spintronics, Nat. Electron. **3**, 360 (2020).

[22] Y.-L. Wang, Z.-L. Xiao, A. Snezhko, J. Xu, L. E. Ocola, R. Divan, J. E. Pearson, G. W. Crabtree, and W.-K. Kwok, Rewritable artificial magnetic charge ice, Science **352**, 962 (2016).

[23] A. Vansteenkiste, J. Leliaert, M. Dvornik, M. Helsen, F. Garcia-Sanchez, and B. V. Waeyenberge, The design and verification of MuMax3, AIP Adv. **4**, 107133 (2014).

[24] A. K. Mondal, C. Banerjee, A. Adhikari, A. K. Chaurasiya, S. Choudhury, J. Sinha, S. Barman, and A. Barman, Spin-texture driven reconfigurable magnonics in chains of connected $Ni_{80}Fe_{20}$ submicron dots, Phys. Rev. B **101**, 224426 (2020).

[25] A. Kumar Mondal, S. Majumder, B. Kumar Mahato, S. Barman, Y. Otani, and A. Barman, Bias field orientation driven reconfigurable magnonics and magnon–magnon coupling in triangular shaped $Ni_{80}Fe_{20}$ nanodot arrays, Nanotechnology **34**, 135701 (2023).

[26] See Supplemental Material at http://link.aps.org/supplemental/10.1103/PhysRevB.109.184433 for Sec. A. Evolution of magnetic histories for RS (reference state), SP (strings phase) -I, and SP-II states, along with spin wave (SW) dispersion for SP-I and SP-II at saturation and Sec. B. Spin wave field dispersion at $\varphi = 0^{\circ}$ and 45°.

[27] D. Kumar, O. Dmytriiev, S. Ponraj, and A. Barman, Numerical calculation of spin wave dispersions in magnetic nanostructures, J. Phys. D: Appl. Phys. **45**, 015001 (2011).

[28] J. Chen, C. Liu, T. Liu, Y. Xiao, K. Xia, G. E. W. Bauer, M. Wu, and H. Yu, Strong interlayer magnon-magnon coupling in magnetic metal-insulator hybrid nanostructures, Phys. Rev. Lett. **120**, 217202 (2018).

[29] Y. Shiota, T. Taniguchi, M. Ishibashi, T. Moriyama, and T. Ono, Tunable magnon-magnon coupling mediated by dynamic dipolar interaction in synthetic antiferromagnets, Phys. Rev. Lett. **125**, 017203 (2020).

[30] K. Y. Guslienko, Magnetic vortex state stability, reversal and dynamics in restricted geometries, J. Nanosci. Nanotechnol. **8**, 2745 (2008).

[31] A. K. Mondal, S. Majumder, S. Sahoo, S. N. Panda, S. Sinha, and A. Barman, Defect-density- and rashba-shift-induced interfacial Dzyaloshinskii–Moriya interaction and spin pumping in single-layer graphene/$Co_{20}Fe_{60}B_{20}$ heterostructures: Implications for new-generation spintronics, ACS Appl. Nano Mater. **5**, 5056 (2022).

[32] B. Hillebrands, C. Mathieu, M. Bauer, S. O. Demokritov, B. Bartenlian, C. Chappert, D. Decanini, F. Rousseaux, and F. Carcenac, Brillouin light scattering investigations of structured permalloy films, J. Appl. Phys. **81**, 4993 (1997).